PHYSICAL REVIEW C **72**, 024006 (2005)

Neutron matter on the lattice with pionless effective field theory

Dean Lee[1] and Thomas Schäfer[1,2]
[1]*Department of Physics, North Carolina State University, Raleigh, North Carolina 27695, USA*
[2]*RIKEN-BNL Research Center, Brookhaven National Laboratory, Upton, New York 11973, USA*

(Received 10 December 2004; published 31 August 2005)

We study neutron matter by combining pionless effective field theory with nonperturbative lattice methods. The neutron contact interaction is determined by zero-temperature scattering data. We simulate neutron matter on the lattice at temperatures of 4 and 8 MeV and densities below one-fifth normal nuclear matter density. Our results at different lattice spacings agree with one another and match bubble-chain calculations at low densities. The equation of state of pure neutron matter obtained from our simulations agrees quantitatively with variational calculations based on realistic potentials.

DOI: 10.1103/PhysRevC.72.024006 PACS number(s): 21.65.+f, 12.39.Fe, 13.75.Cs, 21.30.−x

I. INTRODUCTION

The equation of state of dilute neutron matter is of central importance to the structure and evolution of neutron stars [1,2]. In addition, the neutron matter problem has many interesting physical aspects. Neutron matter has positive pressure at all densities and becomes a superfluid at a sufficiently small temperature. If the density is small, pairing is expected to take place in an S wave, but at a higher density P-wave pairing might be dominant [3]. The neutron matter problem contains a number of very different scales. The neutron scattering length is very large, $a_{nn} \simeq -18$ fm, which implies that the dimensionless parameter $k_F|a_{nn}| \gg 1$ for densities $\rho > 10^{-4}\rho_N$. Here, $k_F = (3\pi^2\rho)^{1/3}$ is the Fermi momentum and $\rho_N \simeq 0.17\ \text{fm}^{-3}$ is the saturation density of nuclear matter. The effective range, on the other hand, is of natural size, $r_{nn} \simeq 2.8$ fm. As a consequence, the parameter $k_F|r_{nn}|$ is neither large nor small for densities $\rho \sim \rho_N$.

If the density is very small, $\rho < 0.1\rho_N$, then $k_F|r_{nn}|$ is a small parameter and neutron matter is close to the limit in which $k_F|a_{nn}| \to \infty$ and $k_F|r_{nn}| \to 0$. In this limit dimensional analysis implies that the energy per particle and the gap have to be proportional to the Fermi energy:

$$\frac{E}{A} = \xi \frac{3}{5}\frac{k_F^2}{2m}, \qquad \Delta = \zeta \frac{k_F^2}{2m}. \tag{1}$$

The determination of the two dimensionless parameters ξ and ζ is a fascinating nonperturbative problem that has received a lot of attention recently. This interest was fueled by experimental advances in creating cold, dilute gases of fermionic atoms tuned to be near a Feshbach resonance [4–8].

The traditional approach to the neutron matter problem is based on the assumption that nucleons can be treated as nonrelativistic point particles interacting mainly by means of two-body potentials. The two-body potentials are fitted to experimental data on nucleon-nucleon scattering. One addresses the many-body problem by solving the many-body Schrödinger equation by using variational methods or the Green's function Monte Carlo methods guided by variational wave functions [9,10].

Even though this method has been very successful, it is desirable to seek an alternative approach that is more directly related to QCD, systematically improvable, and that lends itself to numerical studies that do not rely on variational wave functions. Such an approach is provided by effective field theory (EFT). The use of EFT methods in nuclear physics was pioneered by Weinberg [11]. Over the past few years EFT methods have been applied successfully to the study of two- and three-body systems at low energy [12–14]. Nuclear and neutron matter were studied by use of a perturbative expansion in powers of the Fermi momentum [15] and by use of lattice simulations [16,17].

In this paper we study dilute neutron matter by using a nuclear EFT on the lattice. Because we are interested in densities below nuclear matter saturation density we assume that the relevant momenta are smaller than the pion mass and that we can use an EFT that contains only neutrons. In this work we limit ourselves to the lowest-order effective Lagrangian that contains a single four-fermion contact interaction with no derivatives that is adjusted to the neutron-neutron scattering length. This effective theory is sufficient for investigating universal properties in the limit $k_F|a_{nn}| \to \infty$, $k_F|r_{nn}| \to 0$. An important advantage of the model is the fact that in the case of an attractive interaction there is no sign problem at finite density [18]. As a consequence, it can be simulated efficiently by standard hybrid Monte Carlo (HMC) algorithms [19]. This model is known in the condensed-matter literature as the three-dimensional attractive Hubbard model [20–22]. However, we are interested in a rather unusual limit of the Hubbard model, in which the model approaches a continuum EFT. In our case the Hubbard model parameters are tuned so that the two-body scattering length is infinite (or nearly so) and the lattice spacing and filling fraction tend to zero while keeping the physical density finite.

The paper is organized as follows. In Secs. II–IV we introduce the lattice theory. In Sec. V we discuss how to determine the coefficient of the four-fermion interaction by matching to the two-body scattering length. In Sec. VI we study a low-density approximation to the partition function based on summing particle-particle chains. In Sec. VII we describe our HMC method. Numerical results for the neutron density, the energy per particle, and the equation of state are given in Secs. VIII–XII.

0556-2813/2005/72(2)/024006(12)/$23.00

II. NOTATION

Before describing the physics we first define some notation we use throughout our discussion. We let $\vec{n}$ represent integer-valued lattice vectors on our $3+1$ dimensional space-time lattice. We use a subscripted "s," as in $\vec{n}_s$, to represent purely spatial lattice vectors. We use subscripted indices such as i, j for the two spin components of the neutron, $\uparrow$ and $\downarrow$. We let $\hat{0}$ be the unit lattice vector in the time direction and let $\hat{l}_s = \hat{1}, \hat{2}, \hat{3}$ be the corresponding unit lattice vectors in the spatial directions. A summation symbol such as

$$\sum_{l_s} \tag{2}$$

implies a summation over values $l_s = 1, 2, 3$.

We take the neutron mass to be 939 MeV and normal nuclear matter density to be 0.17 fm^{-3}. We let a be the lattice spacing in the spatial direction and L be the number of lattice sites in each spatial direction. a_t is the lattice spacing in the temporal direction and L_t is the number of lattice sites in the temporal direction. We let α_t be the ratio between lattice spacings, where

$$\alpha_t = \frac{a_t}{a}. \tag{3}$$

Throughout we use dimensionless parameters and operators, which correspond with physical values multiplied by the appropriate power of a. In the end, however, we report final results in physical units such as mega-electron-volts or inverse cubic femtometers. In cases in which there may be confusion, we use the subscript "phys" to identify quantities in physical units.

We use a, $a^\dagger$ to represent annihilation and creation operators for the neutron, whereas c, c^* indicate the corresponding Grassmann variables in the path-integral representation. We let m_N be the mass of the neutron and μ be the neutron chemical potential. For the neutron fields we apply periodic boundary conditions in the spatial directions and antiperiodic boundary conditions in the temporal direction. For each neutron momentum we use the notation

$$\vec{k}_* = \left(\frac{2\pi}{L_t}k_0, \frac{2\pi}{L}k_1, \frac{2\pi}{L}k_2, \frac{2\pi}{L}k_3\right), \tag{4}$$

where k_1, k_2, and k_3 are integers and k_0 is an odd half-integer. In physical units the momentum is

$$\vec{k}_{\text{phys}} = \left(k_{*0}a_t^{-1}, k_{*1}a^{-1}, k_{*2}a^{-1}, k_{*3}a^{-1}\right). \tag{5}$$

Unless otherwise indicated, our momentum labels follow this convention. For convenience we also define

$$h = \frac{\alpha_t}{2m_N}, \tag{6}$$

and

$$\omega_k = 6h - 2h\sum_{l_s}\cos(k_{*l_s}). \tag{7}$$

We let $D^{\text{free}}(\vec{k})\delta_{ij}$ be the free-neutron propagator. For notational convenience the spin-conserving δ_{ij} in the neutron propagator is implicit. The self-energy $\Sigma(\vec{k})$ is defined by

$$D^{\text{full}}(\vec{k}) = \frac{D^{\text{free}}(\vec{k})}{1 - \Sigma(\vec{k})D^{\text{free}}(\vec{k})}, \tag{8}$$

where $D^{\text{full}}(\vec{k})$ is the fully interacting propagator.

TABLE I. Shorthand labels for various lattice spacings used.

a^{-1}(MeV)	a_t^{-1}(MeV)	Label
50	24	0
60	32	1
60	48	2
70	64	3
80	72	4

In our plots we use the abbreviation "fc" for free-continuum results, "f" for free-lattice results, "b" for bubble-chain calculations, and "s" for lattice simulations results. In addition to these abbreviations, we will use the shorthand labels shown in Table I for various combinations of spatial and temporal lattice spacings presented in our analysis.

III. FREE NUCLEON

On the lattice, the free-neutron Hamiltonian can be written as

$$\begin{aligned} H_{\bar{N}N} = {} & \sum_{\vec{n}_s,i}\left[\left(m_N - \mu + \frac{3}{m_N}\right)a_i^\dagger(\vec{n}_s)a_i(\vec{n}_s)\right] \\ & - \frac{1}{2m_N}\sum_{\vec{n}_s,l_s,i}[a_i^\dagger(\vec{n}_s)a_i(\vec{n}_s + \hat{l}_s) + a_i^\dagger(\vec{n}_s)a_i(\vec{n}_s - \hat{l}_s)]. \end{aligned} \tag{9}$$

We can approximate the partition function as a Euclidean lattice path integral:

$$Z_G^{\text{free}} = \text{Tr}\exp(-\beta H_{\bar{N}N}) \simeq z_0^{\text{free}}\int DcDc^*\exp(-S^{\text{free}}), \tag{10}$$

where z_0^{free} is a constant and

$$\begin{aligned} S^{\text{free}} = {} & \sum_{\vec{n},i}[c_i^*(\vec{n})c_i(\vec{n}+\hat{0}) - e^{-(m_N-\mu)\alpha_t} \\ & \times (1-6h)c_i^*(\vec{n})c_i(\vec{n})] - he^{-(m_N-\mu)\alpha_t} \\ & \times \sum_{\vec{n},l_s,i}[c_i^*(\vec{n})c_i(\vec{n}+\hat{l}_s) + c_i^*(\vec{n})c_i(\vec{n}-\hat{l}_s)]. \end{aligned} \tag{11}$$

We have taken a slightly different form than that used in [17]. Instead of the e^{-6h} that appears in [17], we use the more standard $1-6h$ as the coefficient multiplying $c_i^*(\vec{n})c_i(\vec{n})$.

It is conventional to define a new normalization for c_i:

$$c_i' = c_i e^{-(m_N-\mu)\alpha_t}. \tag{12}$$

Then

$$Z_G^{\text{free}} \simeq z_0^{\text{free}}e^{-2(m_N-\mu)\beta L^3}\int Dc'Dc^*\exp(-S^{\text{free}}), \tag{13}$$

where

$$S^{\text{free}} = \sum_{\vec{n},i}[e^{(m_N-\mu)\alpha_t}c_i^*(\vec{n})c_i'(\vec{n}+\hat{0}) - (1-6h)c_i^*(\vec{n})c_i'(\vec{n})] - h\sum_{\vec{n},l_s,i}[c_i^*(\vec{n})c_i'(\vec{n}+\hat{l}_s) + c_i^*(\vec{n})c_i'(\vec{n}-\hat{l}_s)]. \tag{14}$$

In momentum space we have

$$S^{\text{free}} = \sum_{\vec{k},i}\tilde{c}_i^*(-\vec{k})\tilde{c}_i'(\vec{k})\left[e^{-ik_{*0}+(m_N-\mu)\alpha_t} - (1-6h) - 2h\sum_{l_s}\cos(k_{*l_s})\right]. \tag{15}$$

The free-neutron correlation function on the lattice is

$$\frac{\int Dc'Dc^*c_i'(\vec{n})c_i^*(0)\exp(-S^{\text{free}})}{\int Dc'Dc^*\exp(-S^{\text{free}})} = \frac{1}{L_tL^3}\sum_{\vec{k}}e^{-i\vec{k}_*\cdot\vec{n}}D^{\text{free}}(\vec{k}) \tag{16}$$

(no sum over i), where the free-neutron propagator is

$$D^{\text{free}}(\vec{k}) = \frac{1}{e^{-ik_{*0}+(m_N-\mu)\alpha_t} - (1-6h) - 2h\sum_{l_s}\cos(k_{*l_s})} = \frac{1}{e^{-ik_{*0}+(m_N-\mu)\alpha_t} - 1 + \omega_k}. \tag{17}$$

IV. NEUTRON CONTACT TERM

There are two contact interactions at lowest order in the effective theory of nucleons without pions. However, because we are considering pure neutron matter, this reduces to one contact interaction of the form

$$H_{\bar{N}N\bar{N}N} = C\sum_{\vec{n}_s}a_\uparrow^\dagger(\vec{n}_s)a_\uparrow(\vec{n}_s)a_\downarrow^\dagger(\vec{n}_s)a_\downarrow(\vec{n}_s). \tag{18}$$

Because

$$\exp\left[-\frac{C\alpha_t}{2}(a_\uparrow^\dagger a_\uparrow + a_\downarrow^\dagger a_\downarrow)^2\right] = \sqrt{\frac{1}{2\pi}}\int_{-\infty}^{\infty}ds\exp\left[-\frac{1}{2}s^2 + s\sqrt{-C\alpha}(a_\uparrow^\dagger a_\uparrow + a_\downarrow^\dagger a_\downarrow)\right], \tag{19}$$

we can write

$$\exp(-C\alpha_t a_\uparrow^\dagger a_\uparrow a_\downarrow^\dagger a_\downarrow) = \sqrt{\frac{1}{2\pi}}\int_{-\infty}^{\infty}ds\exp\left[-\frac{1}{2}s^2 + \left(s\sqrt{-C\alpha} + \frac{C\alpha_t}{2}\right)\times(a_\uparrow^\dagger a_\uparrow + a_\downarrow^\dagger a_\downarrow)\right]. \tag{20}$$

With this interaction the partition function can be approximated by

$$Z_G = \text{Tr}\exp[-\beta(H_{\bar{N}N} + H_{\bar{N}N\bar{N}N})] \simeq z_0\int DsDcDc^*\exp\left[-S\right], \tag{21}$$

where z_0 is a constant and

$$S = \sum_{\vec{n},i}\left[e^{(m_N-\mu)\alpha_t}c_i^*(\vec{n})c_i'(\vec{n}+\hat{0}) - e^{\sqrt{-C\alpha_t}s(\vec{n})+\frac{C\alpha_t}{2}}\times(1-6h)c_i^*(\vec{n})c_i'(\vec{n})\right] - h\sum_{\vec{n},l_s,i}[c_i^*(\vec{n})c_i'(\vec{n}+\hat{l}_s) + c_i^*(\vec{n})c_i'(\vec{n}-\hat{l}_s)] + \frac{1}{2}\sum_{\vec{n}}s^2(\vec{n}). \tag{22}$$

This lattice action is quite simple, and in the future it may be worth considering improved actions to reduce discretization errors. Nevertheless our lattice action maintains some important properties. One property is that the chemical potential μ is coupled to an exactly conserved neutron number operator. This is clear because μ appears in the same manner as a temporal gauge link. Another feature is that in the limit as $m_N \to \infty$, we find

$$\text{Tr}\exp[-\beta(H_{\bar{N}N} + H_{\bar{N}N\bar{N}N})] = z_0\int DsDcDc^*\exp(-S) + O\left(m_N^{-2}\right). \tag{23}$$

Therefore any dependence on the temporal lattice spacing is suppressed by a factor of m_N^{-2}. This makes it possible to take the static neutron limit as a precision test of the simulation results. We have found this test quite useful in the process of code development and checking.

V. DETERMINING COEFFICIENTS

The interaction coefficient C must be determined for various lattice spacings a and a_t. We do this by summing all bubble-chain diagrams contributing to neutron-neutron scattering, as shown in Fig. 1. The next step is to locate the pole in the scattering amplitude and compare with Lüscher's formula for energy levels in a finite periodic box [23,24]:

$$E_0 = \frac{4\pi a_{\text{scatt}}}{m_NL^3}\left(1 - c_1\frac{a_{\text{scatt}}}{L} + c_2\frac{a_{\text{scatt}}^2}{L^2} + \cdots\right), \tag{24}$$

where $c_1 = -2.837297$, and $c_2 = 6.375183$. We then tune the coefficient C to give the physically measured $^1S_0$ scattering length. Because this scattering length is much larger than any other length scale, we are in essence probing the universal behavior of interacting fermions at infinite scattering length. For our results we have used $a_{\text{scatt}}^{^1S_0} \simeq -24$ fm, though using the value of -18 fm specific for neutron-neutron scattering changes the operator coefficient by only 1%.

The full bubble chain will have a pole when the amplitude for a single bubble times one vertex coefficient equals 1. We take the center-of-mass frame and let the total incoming

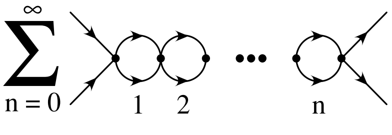

FIG. 1. Bubble-chain diagrams contributing to neutron-neutron scattering.

momentum of the two neutrons in physical units be

$$\vec{p}_{\text{phys}} = \left(p_{*0}a_t^{-1}, 0, 0, 0\right). \tag{25}$$

Because the physical pole occurs in Minkowski space, in the end p_0 will be imaginary. If we set $\mu = 0$, then the amplitude for one bubble times one vertex coefficient is

$$(1-6h)^2(e^{-C\alpha_t}-1)B(p_0), \tag{26}$$

where

$$B(p_0) = \frac{1}{L^3 L_t}\sum_{\vec{k}} \frac{1}{e^{m_N\alpha_t}e^{-ip_{*0}/2}e^{-ik_{*0}} - 1 + \omega_k} \times \frac{1}{e^{m_N\alpha_t}e^{-ip_{*0}/2}e^{ik_{*0}} - 1 + \omega_k}, \tag{27}$$

and the condition for the location of the pole is

$$B(p_0) = \frac{1}{(1-6h)^2(e^{-C\alpha_t}-1)}. \tag{28}$$

By the definition of ω_k in Eq. (7) we see that $0 \leqslant \omega_k \leqslant 12h$. We assume that the lattice spacing in the temporal direction is sufficiently small so that $h \leqslant 1/6$. In practice this presents no problem because m_N is quite large. We then have

$$0 \leqslant \omega_k \leqslant 2, \tag{29}$$

$$-1 \leqslant 1 - \omega_k \leqslant 1. \tag{30}$$

We now make a variable transformation:

$$z = e^{-ik_{*0}} = e^{-i\frac{2\pi}{L_t}k_0}. \tag{31}$$

We also take the zero-temperature limit, $L_t \to \infty$ and convert from the discrete sum over k_0 to an integral clockwise over the unit circle in z by using

$$dz = -i\frac{2\pi}{L_t}z\,dk_0, \tag{32}$$

$$dk_0 = i\frac{L_t}{2\pi z}dz. \tag{33}$$

We then find

$$\begin{aligned} B(p_0) &= \frac{i}{2\pi L^3}\sum_{k_1,k_2,k_3}\oint \frac{dz}{z(e^{m_N\alpha_t}e^{-ip_{*0}/2}z - 1 + \omega_k)(e^{m_N\alpha_t}e^{-ip_{*0}/2}z^{-1} - 1 + \omega_k)} \\ &= \frac{i}{2\pi L^3}\sum_{k_1,k_2,k_3}\oint \frac{dz}{[e^{m_N\alpha_t}e^{-ip_{*0}/2}z - (1-\omega_k)][e^{m_N\alpha_t}e^{-ip_{*0}/2} - (1-\omega_k)z]} \\ &= -\frac{i}{2\pi L^3}\sum_{k_1,k_2,k_3}\oint \frac{e^{-m_N\alpha_t}e^{ip_{*0}/2}(1-\omega_k)^{-1}dz}{[z - e^{-m_N\alpha_t}e^{ip_{*0}/2}(1-\omega_k)][z - e^{m_N\alpha_t}e^{-ip_{*0}/2}(1-\omega_k^{-1}])}. \end{aligned} \tag{34}$$

When $\text{Re}(ip_{*0}\alpha_t^{-1}) < 2m_N$, we pick up the residue at $e^{-m_N\alpha_t}e^{ip_{*0}/2}(1-\omega_k)$, and the amplitude is

$$\begin{aligned} B(p_0) &= -\frac{i}{2\pi L^3}\sum_{k_1,k_2,k_3}\frac{-2\pi i(1-\omega_k)^{-1}}{(1-\omega_k) - e^{2m_N\alpha_t}e^{-ip_{*0}}(1-\omega_k)^{-1}} \\ &= -\frac{i}{2\pi L^3}\sum_{k_1,k_2,k_3}\frac{-2\pi i}{(1-\omega_k)^2 - e^{2m_N\alpha_t}e^{-ip_{*0}}} \\ &= \frac{1}{L^3}\sum_{k_1,k_2,k_3}\frac{1}{e^{2m_N\alpha_t}e^{-ip_{*0}} - 1 + 2\omega_k - \omega_k^2}. \end{aligned} \tag{35}$$

Because we are interested in imaginary p_{*0}, we switch variables:

$$E + 2m_N = ip_{*0}\alpha_t^{-1}, \tag{36}$$

$$e^{-ip_{*0}} = e^{-\alpha_t(E+2m_N)}, \tag{37}$$

where E is the energy in Minkowski space, with rest energy excluded. Finally we get

$$B(E) = \frac{1}{L^3}\sum_{k_1,k_2,k_3}\frac{1}{e^{-\alpha_t E} - 1 + 2\omega_k - \omega_k^2}, \tag{38}$$

and the pole in the bubble-chain sum occurs when

$$B(E) = \frac{1}{(1-6h)^2(e^{-C\alpha_t}-1)}. \tag{39}$$

Using Eq. (24) we can determine C for various spatial and temporal lattice spacings. Results for the lattice spacings used in the simulations presented here are shown in Table II. We have also determined $dC/d\alpha_t$, which we will need when computing the average energy by varying β with fixed L_t.

VI. BUBBLE-CHAIN SUMMATION

In this section we discuss a simple semianalytic calculation that we use to compare with the results of our simulations.

TABLE II. Contact potential coefficients (MeV^{-2}).

a^{-1}(MeV)	a_t^{-1}(MeV)	C(MeV$^{-2)}$	$\frac{dC}{d\alpha_t}$
50	24	-11.6×10^{-5}	-2.21×10^{-5}
60	32	-10.1×10^{-5}	-2.31×10^{-5}
60	48	-8.75×10^{-5}	-1.91×10^{-5}
70	64	-7.58×10^{-5}	-1.92×10^{-5}
80	72	-6.96×10^{-5}	-2.04×10^{-5}

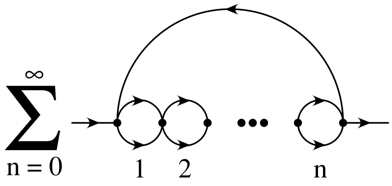

FIG. 2. Bubble-chain diagrams contributing to the neutron self-energy.

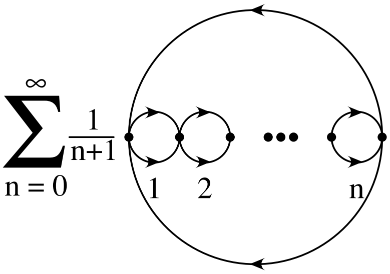

FIG. 3. Bubble-chain diagrams contributing to the logarithm of the partition function.

At $T = 0$ and if $k_F|a_{nn}|$ is small the energy and particle densities can be calculated as an expansion in $k_F|a_{nn}|$. If the scattering length a_{nn} is small this is equivalent to a perturbative expansion in the coupling constant C. If a_{nn} is not small then an infinite set of particle-particle bubbles has to be summed. This is particularly obvious in the lattice cutoff scheme employed in this work. Because the coupling constant C is fixed by the matching of the particle-particle bubble sum to the experimental scattering length at a given lattice spacing, a perturbative expansion of the equation of state in powers of C will not be cutoff independent. An approximation scheme that will reproduce the lowest-order $k_F a_{nn}$ expansion is the bubble-chain summation shown in Figs. 2 and 3.

The problem at $T = 0$ is that the scattering length is very large, and the expansion in $k_F|a_{nn}|$ is not useful unless the density is extremely small, $\rho < 10^{-4}\rho_N$. When $k_F|a_{nn}|$ is not small then corrections must be summed to all orders, and it is not obvious that there is any subset of diagrams that can approximate the full nonperturbative result. We note, however, that the bubble-chain diagrams contain as a subset the diagrams with the minimum number of hole lines. These diagrams are summed by the low-density hole-line expansion.

The situation is simpler if the temperature T is large compared with the degeneracy temperature $T_F = (3\pi^2\rho)^{2/3}/(2m)$. In this case a new length scale, the thermal wavelength or localization length, appears:

$$\lambda_T = \sqrt{\frac{2\pi}{m_N T}}. \tag{40}$$

This length scale acts as an infrared regulator, cutting off long-distance correlations beyond this scale. In particular, it regulates the neutron-neutron scattering amplitude near threshold by giving the function $B(E)$ in Eq.(38) a correction of order $O(\lambda_T^{-1})$. The net effect is that neutrons now have an effective scattering length of

$$|a_{\text{eff}}| \sim \min(|a_{nn}|, \lambda_T). \tag{41}$$

The expansion in $a_{\text{eff}}^3\rho$ converges as long as $a_{\text{eff}}^3\rho < 1$, which is equivalent to $T > T_F$. In the following discussion we compute the bubble-chain diagrams shown in Figs. 2 and 3.

The bubble-chain diagrams in the neutron self-energy form a geometric series. The sum is given by

$$\Sigma(\vec{q}) = -(1-6h)^2(e^{-C\alpha_t}-1) \times \frac{1}{L^3L_t}\sum_{\vec{p}}\frac{D^{\text{free}}(\vec{p}-\vec{q})}{1-(1-6h)^2(e^{-C\alpha_t}-1)B(\vec{p},\mu)}, \tag{42}$$

where

$$B(\vec{p},\mu) = \frac{1}{L^3L_t}\sum_{\vec{k}}\frac{1}{e^{(m_N-\mu)\alpha_t}e^{-ip_{*0}/2}e^{-ik_{*0}}-1+\omega_{p/2+k}} \times \frac{1}{e^{(m_N-\mu)\alpha_t}e^{-ip_{*0}/2}e^{ik_{*0}}-1+\omega_{-p/2+k}}. \tag{43}$$

We use this to compute the full neutron propagator

$$D^{\text{full}}(\vec{q}) = \frac{D^{\text{free}}(\vec{q})}{1-\Sigma(\vec{q})D^{\text{free}}(\vec{q})}, \tag{44}$$

and the average number of neutrons is

$$A = \frac{1}{\beta}\frac{\partial}{\partial\mu}\ln Z_G = 2L^3\left[1-\frac{e^{(m_N-\mu)\alpha_t}}{L_tL^3}\sum_{\vec{k}}D^{\text{full}}(\vec{k})e^{-ik_{*0}}\right]. \tag{45}$$

In a similar fashion we compute the contribution of bubble-chain diagrams to the logarithm of the partition function. The relevant diagrams are shown in Fig. 3.

The factor is $1/(n+1)$ is due to the cyclical symmetry of the diagram. We find

$$\ln Z_G = \ln Z_G^{\text{free}} + \frac{1}{L_tL^3}\sum_{\vec{p},\vec{q}}\frac{-\ln\left[1-(1-6h)^2(e^{-C\alpha_t}-1)B(\vec{p}+\vec{q},\mu)\right]D^{\text{free}}(\vec{p})D^{\text{free}}(\vec{q})}{B(\vec{p}+\vec{q},\mu)}. \tag{46}$$

From this we can compute the average energy E,

$$E = -\frac{\partial\ln Z_G}{\partial\beta} + (-m_N+\mu)A, \tag{47}$$

where we have subtracted out the rest energy. We calculate the derivative with respect to β at fixed L_t by varying α_t:

$$E = -\frac{1}{L_t}\frac{\partial \ln Z_G}{\partial \alpha_t} + (-m_N + \mu)A. \tag{48}$$

We must take into account the dependence of C on α_t, and $dC/d\alpha_t$ for various lattice spacings are shown in Table II.

VII. COMPUTATIONAL METHODS

We use the HMC algorithm [25] to generate field configurations. Roughly 10^5 five-step HMC trajectories were run, split across nine processors running completely independent trajectories. Averages and errors were computed by comparison of the results of each processor. Although the HMC algorithm has become standard in lattice QCD, it may not be so well known in the general nuclear theory community. We therefore include a brief overview of the method as applied to our simulation.

We want to sample the partition function,

$$Z_G \propto \int DsD\psi D\psi^* \exp[-\psi_i^* Q'_{ij}(s)\psi_j - V(s)], \tag{49}$$

where the s_α's are bosonic fields and the ψ_i's are fermionic fields. We use a prime, as we will redefine Q'_{ij} shortly. We can rewrite this as a bosonic path integral,

$$Z_G \propto \int DsD\phi D\phi^* \exp[-S'(\phi, s)], \tag{50}$$

where

$$S'(\phi, s) = \phi_i^* Q'^{-1}_{ij}(s)\phi_j + V(s). \tag{51}$$

The ϕ_i's are bosonic fields and are called pseudofermion fields. The partition function can be written as

$$Z_G \propto \int DsDpD\phi D\phi^* \exp\left[-H(\phi, s, p)\right], \tag{52}$$

where

$$H(\phi, s, p) = S'(\phi, s) + \tfrac{1}{2}p_\alpha p_\alpha. \tag{53}$$

We note that

$$\begin{aligned}\frac{\partial S'(\phi, s)}{\partial s_\alpha} &= \phi_i^* \frac{\partial Q'^{-1}_{ij}(s)}{\partial s_\alpha}\phi_j + \frac{\partial V(s)}{\partial s_\alpha}\\ &= -\phi_i^* Q'^{-1}_{ij}(s)\frac{\partial Q'_{jk}(s)}{\partial s_\alpha}Q'^{-1}_{kl}(s)\phi_l + \frac{\partial V(s)}{\partial s_\alpha}.\end{aligned} \tag{54}$$

In our case the determinant of Q' is real and nonnegative. We can therefore replace Q'_{ij} with a positive semidefinite Hermitian matrix Q_{ij}, with the same determinant. In our case Q'_{ij} has the block-diagonal structure

$$Q' = \begin{bmatrix} K & 0 \\ 0 & K \end{bmatrix}, \tag{55}$$

one block for the up spins and one block for the down spins. Clearly K_{ij} is a matrix with half the dimension of Q'_{ij}. If we let

$$Q = K^\dagger K, \tag{56}$$

then

$$Q^{-1} = K^{-1}(K^\dagger)^{-1} \tag{57}$$

and

$$\det Q = \det Q'. \tag{58}$$

So now instead of $S'(\phi, s)$ we can use

$$\begin{aligned}S(\phi, s) &= \phi_i^* Q^{-1}_{ij}(s)\phi_j + V(s)\\ &= \xi_j^*(s)\xi_j(s) + V(s),\end{aligned} \tag{59}$$

where

$$\xi_i = (K^\dagger)^{-1}_{ij}\phi_j, \tag{60}$$

$$\phi_i = (K^\dagger)_{ij}\xi_j. \tag{61}$$

When we compute the derivative with respect to s_α, we have

$$\begin{aligned}\frac{\partial}{\partial s_\alpha}[K^{-1}(K^\dagger)^{-1}] &= -K^{-1}\frac{\partial K}{\partial s_\alpha}K^{-1}(K^\dagger)^{-1}\\ &\quad - K^{-1}(K^\dagger)^{-1}\frac{\partial K^\dagger}{\partial s_\alpha}(K^\dagger)^{-1}.\end{aligned} \tag{62}$$

Let us define

$$\eta_i = K^{-1}_{ij}\xi_j. \tag{63}$$

Then

$$\phi_i^* \frac{\partial}{\partial s_\alpha}[K^{-1}(K^\dagger)^{-1}]_{ij}\phi_j = -\xi_i^*\left[\frac{\partial K}{\partial s_\alpha}\right]_{ij}\eta_j - \eta_i^*\left[\frac{\partial K^\dagger}{\partial s_\alpha}\right]_{ij}\xi_j. \tag{64}$$

Therefore

$$\frac{\partial S(\phi, s)}{\partial s_\alpha} = -\xi_i^*\left[\frac{\partial K}{\partial s_\alpha}\right]_{ij}\eta_j - \eta_i^*\left[\frac{\partial K^\dagger}{\partial s_\alpha}\right]_{ij}\xi_j + \frac{\partial V(s)}{\partial s_\alpha}. \tag{65}$$

The steps for the HMC algorithm are now as follows.

Step 1: Select an arbitrary initial real-valued configuration s_α^0.

Step 2: Select a complex-valued configuration ξ_j according to the Gaussian random distribution,

$$P(\xi_j) \propto \exp(-|\xi_j|^2), \tag{66}$$

and let

$$\phi_i = (K^\dagger)_{ij}\xi_j, \tag{67}$$

$$\eta_i = K^{-1}_{ij}\xi_j. \tag{68}$$

Step 3: Select real-valued p_α^0 according to the Gaussian random distribution

$$P\left(p_\alpha^0\right) \propto \exp\left[-\frac{1}{2}\left(p_\alpha^0\right)^2\right]. \tag{69}$$

Step 4: Let

$$s_\alpha(0) = s_\alpha^0, \tag{70}$$

and

$$\begin{aligned}\tilde{p}_\alpha(0) = p_\alpha^0 - \frac{\varepsilon}{2}\Bigg[&-\xi_i^*\left[\frac{\partial K}{\partial s_\alpha}\right]_{ij}\eta_j\\ &- \eta_i^*\left[\frac{\partial K^\dagger}{\partial s_\alpha}\right]_{ij}\xi_j + \frac{\partial V(s)}{\partial s_\alpha}\Bigg]_{s=s^0},\end{aligned} \tag{71}$$

for some small positive ε.

Step 5: For $n = 0, 1, \ldots, N-1$, let

$$s_\alpha(n+1) = s_\alpha(n) + \varepsilon \tilde{p}_\alpha(n), \tag{72}$$

$$\begin{aligned}\tilde{p}_\alpha(n+1) = \tilde{p}_\alpha(n) - \varepsilon \Bigg[-\xi_i^* \left[\frac{\partial K}{\partial s_\alpha}\right]_{ij} \eta_j \\ - \eta_i^* \left[\frac{\partial K^\dagger}{\partial s_\alpha}\right]_{ij} \xi_j + \frac{\partial V(s)}{\partial s_\alpha} \Bigg]_{s=s(n+1)}.\end{aligned} \tag{73}$$

Step 6: Let

$$\begin{aligned}p_\alpha(N) = \tilde{p}_\alpha(N) + \frac{\varepsilon}{2} \Bigg[-\xi_i^* \left[\frac{\partial K}{\partial s_\alpha}\right]_{ij} \eta_j \\ - \eta_i^* \left[\frac{\partial K^\dagger}{\partial s_\alpha}\right]_{ij} \xi_j + \frac{\partial V(s)}{\partial s_\alpha} \Bigg]_{s=s(N)}.\end{aligned} \tag{74}$$

Step 7: Select a random number $r \in [0, 1)$. If

$$r < \exp\{-H[\phi, s(N), p(N)] + H(\phi, s^0, p^0)\}, \tag{75}$$

then let

$$s^0 = s(N); \tag{76}$$

otherwise leave s^0 as is. In either case go back to step 2.

The total number of neutrons A is

$$\begin{aligned}A &= \frac{1}{\beta}\frac{\partial}{\partial\mu}\ln Z_G = 2L^3 - \frac{1}{\beta}\frac{\int DsDc'Dc^* \frac{\partial S}{\partial\mu}\exp(-S)}{\int DsDc'Dc^*\exp(-S)} \\ &= 2L^3\left[1 - \frac{e^{(m_N-\mu)\alpha_t}\int DsDc'Dc^* c'_\uparrow(\vec{n}+\hat{0})c^*_\uparrow(\vec{n})\exp(-S)}{\int DsDc'Dc^*\exp(-S)}\right]\end{aligned} \tag{77}$$

for any lattice site $\vec{n}$. Dividing by the volume $V = L^3$ gives the density ρ in lattice units. We compute the total energy using Eq.(48),

$$\begin{aligned}E &= -\frac{1}{L_t}\frac{\partial \ln Z_G}{\partial\alpha_t} + (-m_N+\mu)A \\ &= \frac{1}{L_t}\frac{\int DsDc'Dc^*\frac{\partial S}{\partial\alpha_t}\exp(-S)}{\int DsDc'Dc^*\exp(-S)} + (-m_N+\mu)A,\end{aligned} \tag{78}$$

where we take into account the α_t dependence of C when computing $\partial S/\partial\alpha_t$. We then have

$$E = 2L^3\frac{\int DsDc'Dc^* f(s,c',c^*)\exp(-S)}{\int DsDc'Dc^*\exp(-S)} + (-m_N+\mu)A \tag{79}$$

where

$$\begin{aligned}f(s,c',c^*) = -(m_N-\mu)e^{(m_N-\mu)\alpha_t}c'_\uparrow(\vec{n}+\hat{0})c^*_\uparrow(\vec{n}) \\ + \frac{\partial}{\partial\alpha_t}[e^{\sqrt{-C\alpha_t}s(\vec{n})+\frac{C\alpha_t}{2}}(1-6h)]c'_\uparrow(\vec{n})c^*_\uparrow(\vec{n}) \\ + \frac{1}{2m_N}\sum_{l_s}[c'_\uparrow(\vec{n}+\hat{l}_s)c^*_\uparrow(\vec{n}) + c'_\uparrow(\vec{n}-\hat{l}_s)c^*_\uparrow(\vec{n})]\end{aligned} \tag{80}$$

for any lattice site $\vec{n}$.

VIII. FREE-NEUTRON RESULTS

To better understand our lattice discretization errors, we compare our free-neutron results on the lattice with the continuum free Fermi gas. For a continuum free Fermi gas, the logarithm of the partition function is

$$\ln Z_G^{\text{free}} = \ln Z_{G,\uparrow}^{\text{free}} + \ln Z_{G,\downarrow}^{\text{free}} = 2\ln Z_{G,\uparrow}^{\text{free}}, \tag{81}$$

where the logarithm of the single-spin partition function is

$$\begin{aligned}\ln Z_\uparrow^{\text{free}} &= V\int\frac{d^3\vec{p}}{(2\pi)^3}\ln\left[1+e^{-\beta\left(\frac{\vec{p}^2}{2m_N}+m_N-\mu\right)}\right] \\ &= \frac{V}{2\pi^2}\int_0^\infty dp\,p^2\ln\left[1+e^{-\beta\left(\frac{p^2}{2m_N}+m_N-\mu\right)}\right].\end{aligned} \tag{82}$$

Therefore the energy density is

$$\frac{E_\uparrow^{\text{free}}}{V} = \frac{1}{2\pi^2}\int_0^\infty dp\frac{p^4}{2m_N}\frac{1}{e^{\beta\left(\frac{p^2}{2m_N}+m_N-\mu\right)}+1}, \tag{83}$$

and the number density is

$$\rho_\uparrow^{\text{free}} = \frac{A^{\text{free}}}{V} = \frac{1}{2\pi^2}\int_0^\infty dp\,p^2\frac{1}{e^{\beta\left(\frac{p^2}{2m_N}+m_N-\mu\right)}+1}. \tag{84}$$

We double these to get the results for both spins. In the limit as $\rho^{\text{free}} \to 0$ we find the usual equipartition result for the energy per neutron:

$$\frac{E^{\text{free}}}{A^{\text{free}}} = \frac{3}{2}T. \tag{85}$$

A plot of density versus chemical potential at temperature $T = 8$ MeV is shown in Fig. 4. The energy per neutron at temperature $T = 8$ MeV is shown in Fig. 5. To avoid large cutoff effects, we present only results at densities corresponding with lattice fillings of about one-quarter or less.

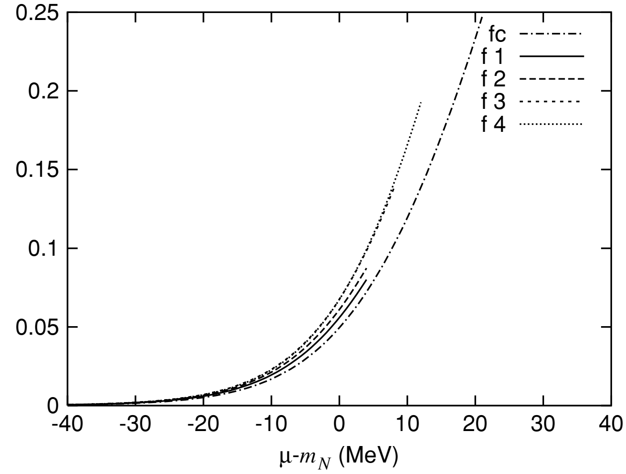

FIG. 4. Density versus chemical potential for free neutrons on the lattice at $T = 8$ MeV and various lattice spacings. The curves labeled f1–f4 refer to the lattice spacings defined in Table I. The curve labeled fc shows the continuum limit for free neutrons.

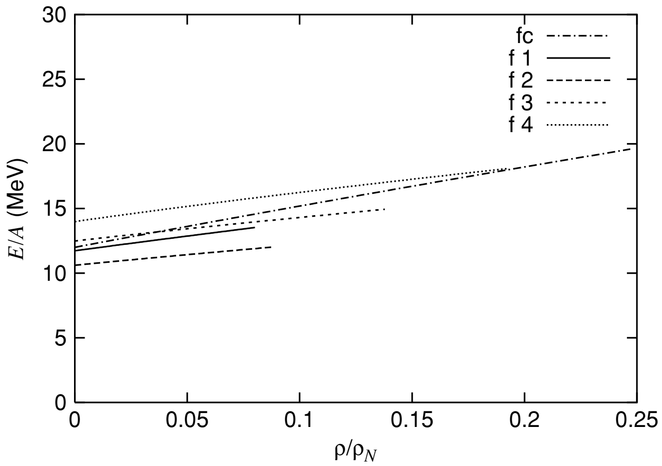

FIG. 5. Energy per neutron versus density for free neutrons on the lattice at $T = 8$ MeV and various lattice spacings.

This is why our data at longer lattice spacings terminate at lower densities.

We see in Figs. 4 and 5 some residual dependence on lattice spacings. Although it is a small effect, it does make it visually confusing to overlay plots for different lattice spacings. We mentioned the possibility of using improved actions to reduce residual lattice discretization error. In this analysis, however, we use a less-expensive route. We simply rescale our densities and energies so that the free-lattice results and free-continuum results agree at $\mu = m_N$:

$$\rho(a, a_t, L, T, \mu) \to \rho(a, a_t, L, T, \mu) \times \frac{\rho^{\text{free}}(a = 0, a_t = 0, L = \infty, T, \mu = m_N)}{\rho^{\text{free}}(a, a_t, L, T, \mu = m_N)}, \quad (86)$$

$$E(a, a_t, L, T, \mu) \to E(a, a_t, L, T, \mu) \times \frac{E^{\text{free}}(a = 0, a_t = 0, L = \infty, T, \mu = m_N)}{E^{\text{free}}(a, a_t, L, T, \mu = m_N)}. \quad (87)$$

The motivation for this adjustment is our empirical observation that the dominant discretization error in ρ and E is a systematic error that depends on the size of the temporal lattice spacing relative to the spatial lattice spacing. The correction is about a 10%–20% effect and seems to be about the same for both the free and fully interacting results. Therefore we apply the same multiplicative adjustment to all lattice results. This includes free-lattice results, bubble-chain diagram results, and lattice simulation results.

IX. VOLUME DEPENDENCE

For the $T = 8$ MeV simulations we use a lattice volume of (13 fm)^3 or larger. For the $T = 4$ MeV simulations we use a lattice volume of (20 fm)^3 or larger. The dimensions of our $L^3 \times L_t$ lattices are shown in Tables III and IV.

We have run simulations at both smaller and larger volumes. In Table V we show the results for $T = 8$ MeV and $\mu - m_N = -2$ MeV, $a^{-1} = 60$ MeV, and $a_t^{-1} = 32$ MeV. Because we are not changing the lattice spacings for this comparison we can compare raw data without rescaling ρ and E.

TABLE III. Lattice dimensions for $T = 8$ MeV.

Label	L	L_t
1	4	4
2	4	6
3	5	8
4	6	9

In Table VI we show analogous results for $T = 4$ MeV and $\mu = m_N$, $a^{-1} = 50$ MeV, and $a_t^{-1} = 24$ MeV.

These results suggest that finite-volume effects for the lattice sizes listed in Tables III and IV are smaller than our statistical errors. If we take the volume dependence from the free and bubble-chain calculations as a guide, then the finite-volume errors are well below the 1% level.

X. DENSITY VERSUS CHEMICAL POTENTIAL

In Fig. 6 we plot density versus chemical potential for $T = 8$ MeV, and in Fig. 7 we plot density versus chemical potential for $T = 4$ MeV. In both cases we see agreement among data for different lattice spacings. This suggests that we have properly renormalized the interaction and absorbed the lattice spacing dependence into the scale-dependent interaction coefficient. We observe no phase transitions as a function of chemical potential. We note in particular that we can choose the chemical potential such that the occupation number in the interacting theory remains small. This implies that there is no instability toward a fully occupied ground state. As expected for a theory with attractive interactions the density at a given chemical potential is larger in the interacting theory. We observe that this behavior is well described by the bubble-chain results for $T > T_F$, the low-density regime where we expect agreement.

XI. ENERGY PER NEUTRON VERSUS DENSITY

In Fig. 8 we plot energy per neutron versus density for $T = 8$ MeV, and in Fig. 9 we plot energy per neutron versus density for $T = 4$ MeV. In both cases we see good agreement among data for different lattice spacings. As expected, the energy per particle approaches $1.5T$ in the dilute limit. The energy per particle decreases as a function of density in the regime that we have studied. At small ρ the slope is very steep, which is consistent with the perturbative result for particles that have a large negative scattering length. We

TABLE IV. Lattice dimensions for $T = 4$ MeV.

Label	L	L_t
0	5	6
1	6	8

TABLE V. L dependence for $T = 8$ MeV.

L	$\frac{\rho^{\text{free}}}{\rho_N}$	$\frac{E^{\text{free}}}{A^{\text{free}}}$ (MeV)	$\frac{\rho^{\text{bubble}}}{\rho_N}$	$\frac{E^{\text{bubble}}}{A^{\text{bubble}}}$ (MeV)	$\frac{\rho^{\text{simulation}}}{\rho_N}$	$\frac{E^{\text{simulation}}}{A^{\text{simulation}}}$ (MeV)
3	0.04588	12.582	0.08176	6.514	0.0885(4)	6.19(2)
4	0.04596	12.777	0.08215	6.539	0.0890(2)	6.21(2)
5	0.04600	12.757	0.08217	6.531	0.0886(3)	6.19(2)
6	0.04600	12.756	0.08217	6.531	0.0891(3)	6.20(2)

note, however, that the behavior is not linear, even at very small density. The simulations are very well described by the bubble-chain results for $T > T_F$. We also observe that for the larger densities, $\rho > 0.1\rho_N$ at $T = 8$ MeV and $\rho > 0.03\rho_N$ at $T = 4$ MeV, the energy per particle is smaller than the result for a free-neutron gas at zero temperature. In this regime the Fermi energy of the degenerate system is lower than the temperature. Our results suggest that the parameter ξ defined in Eq. (1) is smaller than 0.5. We should note, however, that the parameter $k_F r_{nn} \sim k_F a$, where a is the lattice spacing, is of the order of 1 and simulations at lower temperature will be required for making more definitive estimates of ξ.

The decrease in the energy per neutron with increasing density does not necessarily imply an instability to neutron clustering. At nonzero temperature, entropy must also be taken into account, and the question of whether phase separation occurs is resolved in the next section when we look at the equation of state.

XII. EQUATION OF STATE

We integrate the density as a function of chemical potential to measure the pressure:

$$P = \frac{T}{V}\ln Z_G = \frac{1}{V}\int_{-\infty}^{\mu} A(\mu')d\mu' = \int_{-\infty}^{\mu} \rho(\mu')d\mu'. \quad (88)$$

We perform the integration by least-squares fitting $\rho(\mu')$ with a function of the form

$$\rho(\mu') = (c_0 + c_1\mu' + c_2\mu'^2)\exp(b\mu'). \quad (89)$$

We can then perform the integration analytically. In Fig. 10 we plot the pressure versus density for $T = 8$ MeV, and in Fig. 11 we plot the pressure versus density for $T = 4$ MeV. In both cases the pressure is a smooth strictly increasing function of density. Therefore we conclude that there is no indication of phase separation.

There are many models we could use to compare with our results. We first consider the results of a variational calculation by Friedman and Pandharipande [9]. They use a realistic Hamiltonian that consists of the Argonne v_{14} interaction supplemented by a three-body force. We have taken the data for different temperatures given in Table IV of [9] and interpolated to obtain the pressure for $T = 4$ MeV and $T = 8$ MeV. The result are shown by the crosses in Figs. 10 and 11. We observe that the agreement with our calculations is remarkably good. There are a number of factors that are likely to contribute to this result. One is the fact that for the low densities considered in the present work explicit pions as well as three-body forces are not important. Another point is that the equation of state appears to be relatively insensitive to effective range corrections that are not taken into account in this work. Indeed, the Green's function Monte Carlo calculations with realistic interactions give an equation of state that is very similar to the result obtained with a very short-range interaction [9,26].

We also show the equation of state for a simple phenomenological model of the equation of state described in [27] and a review article [28]. The model contains a parametrization of the equation of state of symmetric nuclear matter adjusted to the saturation properties and the compressibility. The authors consider three possible functional forms of asymmetry:

$$(\text{version }1) P_{\text{asy}} = 2e_a\rho_N\left(\frac{\rho}{\rho_N}\right)^3\delta^2, \quad (90)$$

$$(\text{version }2) P_{\text{asy}} = e_a\rho_N\left(\frac{\rho}{\rho_N}\right)^2\delta^2, \quad (91)$$

$$(\text{version }3) P_{\text{asy}} = \frac{1}{2}e_a\rho_N\left(\frac{\rho}{\rho_N}\right)^{\frac{3}{2}}\delta^2, \quad (92)$$

where $e_a \simeq 20$ MeV and the asymmetry parameter δ is defined as

$$\delta = \frac{\rho_n - \rho_p}{\rho_n + \rho_p}. \quad (93)$$

The equations of state of the three different models for $T = 8$ MeV and $T = 4$ MeV are shown in Figs. 12 and 13. For

TABLE VI. L dependence for $T = 4$ MeV.

L	$\frac{\rho^{\text{free}}}{\rho_N}$	$\frac{E^{\text{free}}}{A^{\text{free}}}$ (MeV)	$\frac{\rho^{\text{bubble}}}{\rho_N}$	$\frac{E^{\text{bubble}}}{A^{\text{bubble}}}$ (MeV)	$\frac{\rho^{\text{simulation}}}{\rho_N}$	$\frac{E^{\text{simulation}}}{A^{\text{simulation}}}$ (MeV)
4	0.02234	7.349	0.04663	3.474	0.0536(3)	3.33(2)
5	0.02238	7.344	0.04667	3.469	0.0533(2)	3.33(2)
6	0.02238	7.341	0.04666	3.469	0.0530(2)	3.35(2)
7	0.02238	7.341	0.04666	3.469	0.0530(2)	3.35(2)

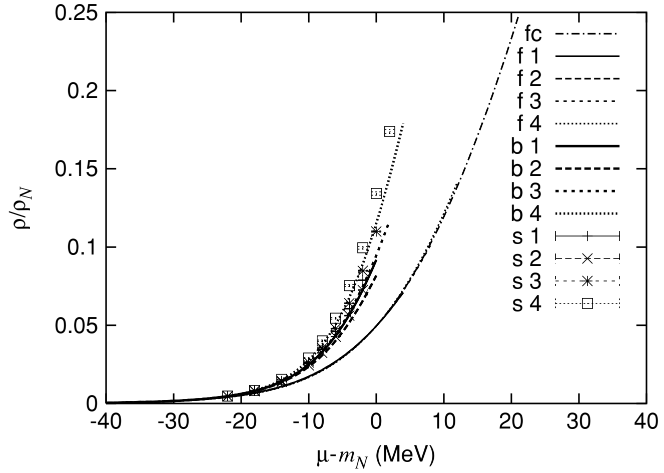

FIG. 6. Density versus chemical potential at $T = 8$ MeV and various lattice spacings. The curves labeled f1–f4 show free-neutron results, b1–b4 show the bubble-chain results, and s1–s4 show numerical simulations. The corresponding lattice spacings are given in Table I.

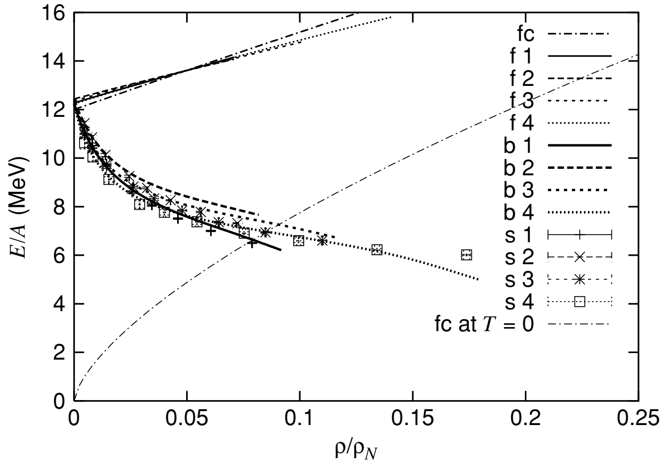

FIG. 8. Energy per neutron versus density at $T = 8$ MeV for various lattice spacings.

comparison, we also show the variational results of Friedman and Pandharipande. We observe that our results, as well as the results of Friedman and Pandharipande, appear to agree most closely with version 3. Further investigations are needed to determine whether other properties of this simple model agree with our lattice simulation results.

XIII. SUMMARY AND CONCLUSIONS

In this work we studied neutron matter by combining pionless EFT at lowest order with nonperturbative lattice methods. To determine the neutron contact interaction we summed bubble-chain diagrams contributing to neutron-neutron scattering at a given lattice spacing. The contact interaction was then adjusted to produce the pole in the amplitude indicated by Lüscher's finite-volume formula for the physical $^1S_0$ scattering length. Having determined the interaction coefficient for various lattice spacings, we then simulated neutron matter on the lattice by using HMC at temperatures 4 and 8 MeV and densities below one-fifth normal nuclear matter density.

We find that our results at different lattice spacings agree with one another. This suggests that the continuum limit exists and that our effective theory is properly renormalized or, more conservatively, that any cutoff dependence is numerically small. For the range of parameters studied in this work we observe no instabilities toward phase separation or toward lattice artifacts such as a completely filled lattice. Although not unexpected, this is not a trivial result because the nonperturbative simulation includes all possible diagrams.

The energy per particle at temperatures $T = 4$ MeV and $T = 8$ MeV shows a steep downward slope at very small

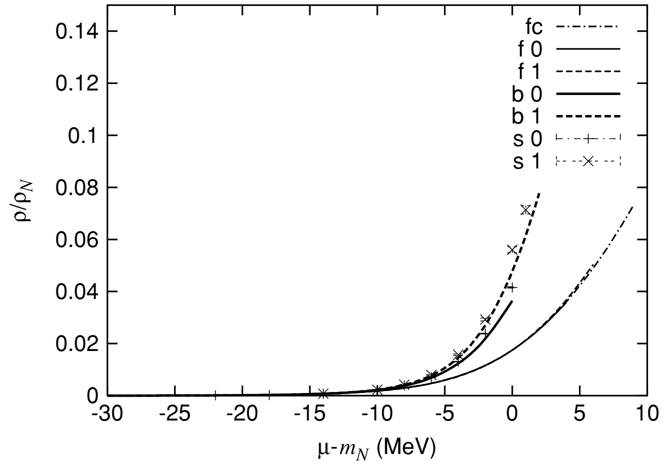

FIG. 7. Density versus chemical potential at $T = 4$ MeV and various lattice spacings.

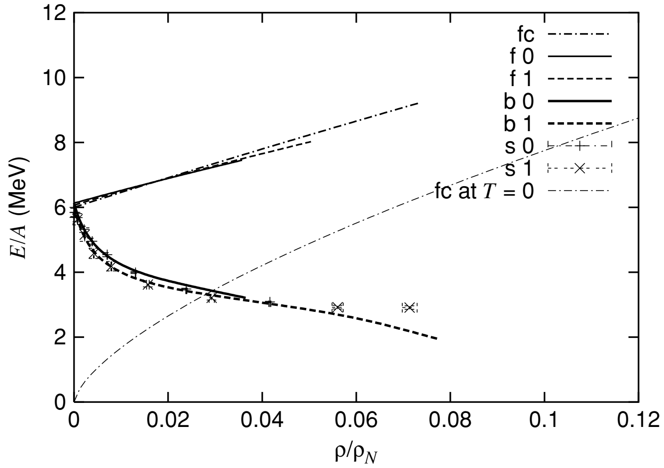

FIG. 9. Energy per neutron versus density at $T = 4$ MeV for various lattice spacings.

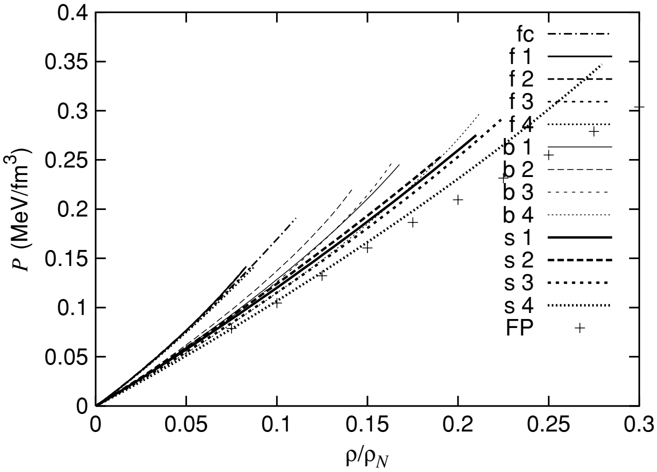

FIG. 10. Pressure versus density at $T = 8$ MeV for various lattice spacings. The crosses show the results of a variational calculation by Friedman and Pandharipande [9].

density, which is a sign of the strong attractive interaction between neutrons. At intermediate densities $\rho \sim 0.1\rho_N$ the energy per particle levels off. This behavior is reproduced quantitatively by our bubble-chain calculations for $T > T_F$. In the future we wish to push our simulations to lower temperatures and determine the universal parameters ξ and ζ for the energy per particle and gap as defined in Eq. (1). Simulations in this regime will require a source term for the dineutron field. We have not seen unambiguous signs of superfluidity in our simulations. This may be related to the fact that, in the regime where T/T_F is of the order of unity, the parameter $k_F a$, where a is the lattice spacing, is not small. As a consequence effective range corrections are probably important. In BCS theory, range corrections as well as higher-order terms in the effective range expansion lead to a substantial suppression of the gap in pure neutron matter [3].

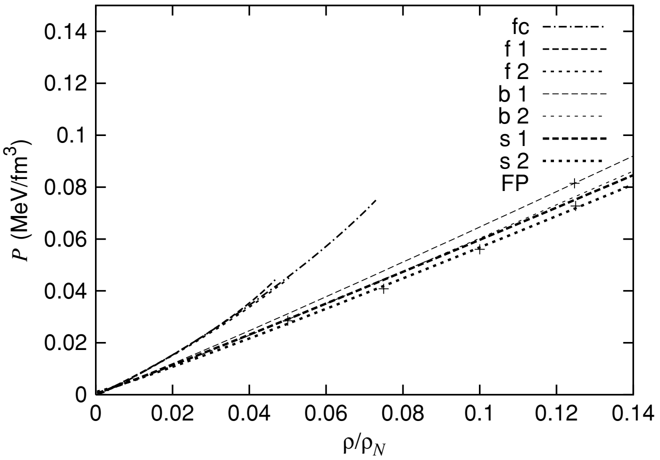

FIG. 11. Pressure versus density at $T = 4$ MeV for various lattice spacings. The crosses show the results of a variational calculation by Friedman and Pandharipande [9].

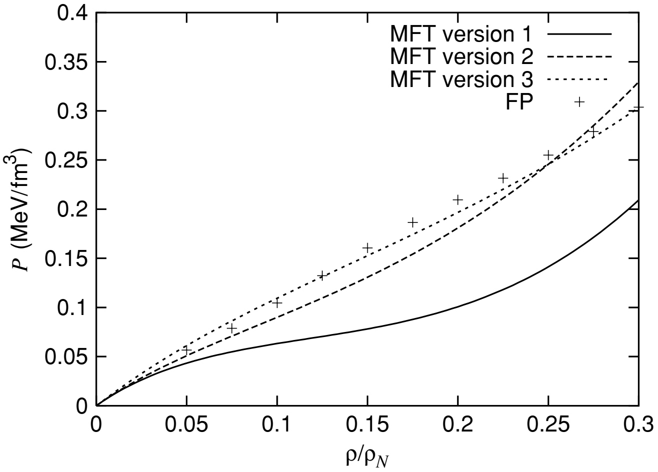

FIG. 12. Pressure versus density at $T = 8$ MeV for the phenomenological equation of state discussed in [27]. The three different curves correspond to different parametrizations of the symmetry energy.

A very small value of T_c/T_F was also obtained in a recent lattice study by Wingate [29].

Our results for the pressure of pure neutron matter agree remarkably well with the variational calculation of Friedman and Pandharipande [9]. In the future it will be interesting to study whether the agreement persists if higher-order terms in the effective Lagrangian or explicit pions are introduced. We have also performed simulations with explicit pions [17], but these data were taken at larger density and temperature. It will also be interesting to study systems with a finite proton fraction. This is easiest in the limit of exact Wigner symmetry, as the leading-order Euclidean action is positive in that case [30].

It will also be interesting to investigate the phase structure of the leading-order effective theory in more detail. To have a

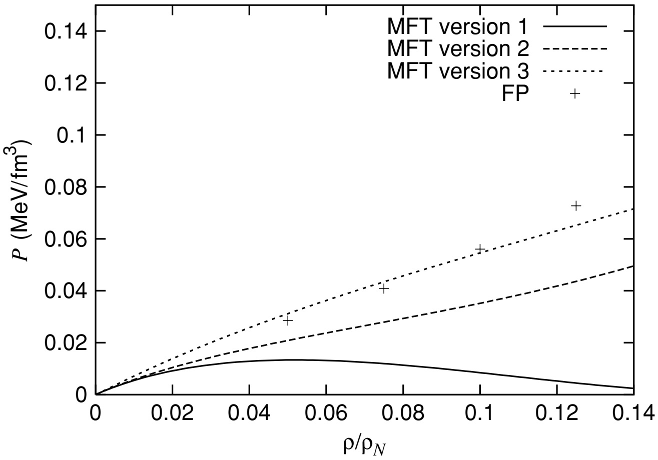

FIG. 13. Pressure versus density at $T = 4$ MeV for the phenomenological equation of state discussed in [27]. The three different curves correspond to different parametrizations of the symmetry energy.

positive Euclidean action the coefficient C of the four-fermion interaction has to be negative. This corresponds to either a negative scattering length or a scattering length that is large and positive [18]. This implies that the effective theory studied in this work can be used to investigate the BCS-BEC crossover in a dilute Fermi gas.

ACKNOWLEDGMENTS

The authors thank Simon Hands and Matthew Wingate for discussions on the hybrid Monte Carlo algorithm. This work was supported in part by U.S. Department of energy grants DE-FG-88ER40388 and DE-FG02-04ER41335.

[1] H. Heiselberg and V. Pandharipande, Annu. Rev. Nucl. Part. Sci. **50**, 481 (2000).
[2] J. M. Lattimer and M. Prakash, Astrophys. J. **550**, 426 (2001).
[3] D. J. Dean and M. Hjorth-Jensen, Rev. Mod. Phys. **75**, 607 (2003).
[4] K. M. O'Hara, S. L. Hemmer, M. E. Gehm, S. R. Granade, and J. E. Thomas, Science **298**, 2179 (2002).
[5] S. Gupta *et al.*, Science **300**, 1723 (2003).
[6] C. A. Regal and D. S. Jin, Phys. Rev. Lett. **90**, 230404 (2003).
[7] T. Bourdel, J. Cubizolles, L. Khayhovich, K. M. F. Magalhaes, S. J. J. M. F. Kokkelmans, G. V. Shlyapnikov, and C. Salomon, Phys. Rev. Lett. **91**, 020402 (2003).
[8] M. E. Gehm, S. L. Hemmer, S. R. Granade, K. M. O'Hara, and J. E. Thomas, Phys. Rev. A **68**, 011401(R) (2003).
[9] B. Friedman and V. R. Pandharipande, Nucl. Phys. **A361**, 502 (1981).
[10] J. Carlson, J. Morales, V. R. Pandharipande, and D. G. Ravenhall, Phys. Rev. C **68**, 025802 (2003).
[11] S. Weinberg, Phys. Lett. **B251**, 288 (1990).
[12] E. Epelbaum, W. Glockle, A. Kruger, and U.-G. Meissner, Nucl. Phys. **A645**, 413 (1999).
[13] S. R. Beane, P. F. Bedaque, W. C. Haxton, D. R. Phillips, and M. J. Savage in *Boris Ioffe Festschrift*, *at the Frontier Particle Physics, Vol. 1*, edited by M. Shifman (World Scientific, Singapore, 2000).
[14] P. F. Bedaque and U. van Kolck, Annu. Rev. Nucl. Part. Sci. **52**, 339 (2002), nucl-th/0203055.
[15] N. Kaiser, S. Fritsch, and W. Weise, Nucl. Phys. **A697**, 255 (2002).
[16] H. M. Müller, S. E. Koonin, R. Seki, and U. van Kolck, Phys. Rev. C **61**, 044320 (2000).
[17] D. Lee, B. Borasoy, and T. Schaefer, Phys. Rev. C **70**, 014007 (2004).
[18] J.-W. Chen and D. B. Kaplan, Phys. Rev. Lett. **92**, 257002 (2004).
[19] M. Wingate, hep-lat/0409060; poster presented at Lattice 2004, Fermilab, Batavia, Illinois, 21–26 June 2004.
[20] A. Sewer, X. Zotos, and H. Beck, Phys. Rev. B **66**, 140504(R) (2002).
[21] M. Capone, C. Castellani, and M. Grilli, Phys. Rev. Lett. **88**, 126403 (2002).
[22] M. Keller, W. Metzner, and U. Schollwock, Phys. Rev. Lett. **86**, 4612 (2001).
[23] M. Lüscher, Commun. Math. Phys. **105**, 153 (1986).
[24] S. R. Beane, P. F. Bedaque, A. Parreno, and M. J. Savage, Phys. Lett. **B585**, 106 (2004).
[25] S. Duane, A. D. Kennedy, B. J. Pendleton, and D. Roweth, Phys. Lett. **B195**, 216 (1987).
[26] S. Y. Chang *et al.*, Nucl. Phys. **A746**, 215 (2004).
[27] B.-A. Li and C. M. Ko, Nucl. Phys. **A618**, 498 (1997).
[28] B.-A. Li, C. M. Ko, and W. Bauer, Int. J. Mod. Phys. E **7**, 147 (1998), nucl-th/9707014.
[29] M. Wingate (2005), cond-mat/0502372.
[30] J.-W. Chen, D. Lee, and T. Schaefer, Phys. Rev. Lett. **93**, 242302 (2004).